Prediction of Majorana edge states from magnetized topological surface states

Xiaoming Zhang [1,*] and Feng Liu [2,†]

[1]*Department of Physics, College of Information Science and Engineering, Ocean University of China, Qingdao, Shandong 266100, China*
[2]*Department of Materials Science and Engineering, University of Utah, Salt Lake City, Utah 84112, USA*

(Received 12 October 2020; revised 9 December 2020; accepted 10 December 2020; published 6 January 2021)

As key signatures of topological superconductors (TSCs), the chiral and helical Majorana edge states (MESs) have received increasing attention recently. One prudent mechanism for realizing the MESs is by magnetizing topological surface states (TSSs) associated with conventional superconductivity. Here we construct comprehensive phase diagrams in the parameter space of magnetization and superconductivity for TSSs, based on tight-binding model analyses. In addition to the chiral MESs hosted by the quantum anomalous Hall (QAH), the half-plateau surface QAH and the zero-plateau QAH states, we find that the axion insulator state can realize helical MES, where the opened Zeeman gaps in two TSSs with antiferromagnetic exchange fields eliminate the requirement of the opposite phases between the superconducting gaps in two TSSs. We also demonstrate that the TSC phase is robust against the increase of interaction between two TSSs when the square of the sum of two superconducting gaps is smaller than that of two Zeeman energies. Furthermore, using first-principles approach, we predict $MnBi_2Te_4/Bi_2Te_3$ film placed on a superconducting substrate to be an ideal experimental platform to realize the chiral MESs within a wide energy range (∼80 meV), which persist even down to one quintuple layer of Bi_2Te_3. Our findings shed light on fundamental understanding of TSC phase and paving another avenue to search for TSC materials.

DOI: 10.1103/PhysRevB.103.024405

I. INTRODUCTION

Topological superconductors (TSCs) possess a nontrivial superconducting gap and localized in-gap states that include Majorana bound states (MBSs) at zero energy and one-dimensional (1D) chiral/helical Majorana edge states (MESs). The braiding of MBSs and the propagation of Majorana fermions on chiral MESs may be utilized in topological quantum computation [1–3]. In addition to the well-studied MBSs realized in various experimental platforms under external magnetic field [4–10], the studies of 1D MESs have received increasing attention recently [11–16]. The hybrid system that combines superconductor (SC) with the quantum anomalous Hall (QAH) insulator showed the first realization of chiral MESs [11], which can be understood from the theoretical models of magnetized topological surface states (TSSs) of topological insulators (TIs) [17–20]. An alternative route to chiral MESs employs the superconductivity and the Rashba spin-orbit coupled states (RSOCSs) with time-reversal symmetry breaking [21–23], which has been realized in nanoscale magnetic islands [12,13] and ferromagnet [14] in proximity with SCs. Moreover, signature of helical MESs has been observed in the domain walls of $FeSe_{0.45}Te_{0.55}$ with TSSs [15]. To further advance this emerging field, apparently more complete understanding and new experimental platforms for realizing 1D MESs are highly desirable.

Compared to the RSOCS where the TSC phase exists under the condition of $Z^2 > \Delta^2 + \mu^2$ [Z is the Zeeman energy and μ is the chemical potential that determines position of superconducting gap Δ as shown in Fig. 1(a)] [21–23], the phase diagram of TI thin film with two magnetized TSSs tends to be more complicated. It involves more parameters, including the superconducting gaps ($\Delta_{t/b}$) and exchange fields ($Z_{t/b}$) in the top/bottom TSS, μ, and the interaction (I) between two TSSs. The TSC phase diagrams of the two magnetized TSSs with the same Zeeman energy were constructed [19], which demonstrate that the 1D MESs can be realized by tuning the phase difference between the superconducting gaps of two TSSs. Another work showed the TSC phase remains with only one TSS experiencing the exchange field [20], which indicates that the phase difference in the Zeeman gaps affords an alternative route to tuning the TSC phase. This calls for a further theoretical study to construct TSC phase diagrams in the varying parameter space of Zeeman energy for a given parameter set of superconductivity. It may extend the discovery of TSCs in the diverse electronic phases formed by the magnetized TSSs, including the QAH state [24,25], the half-plateau surface QAH (HPSQAH) state [26], the zero plateau QAH (ZPQAH) state [27,28] and even the axion insulators (AIs) [29].

Moreover, prediction of new TSC candidate materials including the film thickness dependence will be valuable for guiding experiments. We note that the direction and magnitude of exchange fields applied on each TSS can be controlled by changing external magnetic field [30], interfacing TIs with ferromagnetic insulators (FMIs) [31,32], as well as tuning the film thickness. Therefore,

*zxm@ouc.edu.cn
†fliu@eng.utah.edu

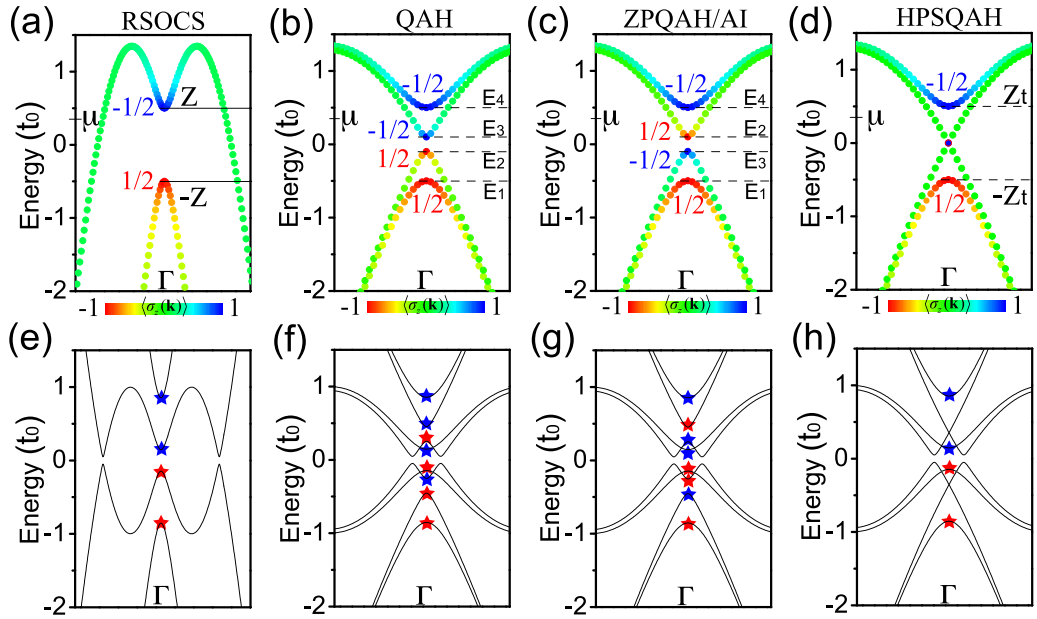

FIG. 1. The electronic band structures of (a) magnetized RSOCS, (b) QAH, (c) ZPQAH (or AI when $I = 0$), and (d) HPSQAH state, formed by magnetized TSSs. The color represents the expectation value of Pauli matrice σ_z. The marked $1/2$ or $-1/2$ are the Chern number calculated by integrating the Berry coverture around the corresponding gap edge. The superconducting quasiparticle dispersions of (e) magnetized RSOCS, (f) QAH, (g) ZPQAH, and (h) HPSQAH state with the intraorbital spin-singlet pairing condensing at the chemical potential μ that are marked in (a), (b), (c), and (d), respectively. The red (blue) stars indicate the states from which the Chern number $N = 1/2$ $(-1/2)$ mainly comes.

tuning the exchange fields on different TSSs, rather than the phase difference of the superconducting gaps, may provide another feasible experimental approach to realize the 1D MESs, especially considering the availability of fabricating various heterostructures consisting of TIs and FMIs [33], e.g., $Bi_2Te_3/MnBi_2Te_4$ [25,34], Bi_2Se_3/Bi_2MnSe_4 [35], $Bi_2Se_3/MnSe$ [36], Bi_2Se_3/GdN [37], $Bi_2Se_3/BaFe_{12}O_{19}$ [38], $Bi_2Se_3/NiFe$ [39], Bi_2Se_3/EuS [40], $Bi_2Se_3/LaCoO_3$ [41], $Bi_2Te_3/Cr_2Ge_2Te_6$ [42], $(Bi_xSb_{1-x})_2Te_3/Y_3Fe_5O_{12}$ [43], $(Bi_xSb_{1-x})_2Te_3/Tm_3Fe_5O_{12}$ [44], and (Bi; Sb)$_2Te_3/Cr_2Ge_2Te_6$ [45]. One prerequisite is that the magnetic proximity effects of FMIs only open exchange gaps near the Dirac cone of TSSs, but maintain the opposite spin polarization at **k** and **–k** points to ensure a spin-singlet superconducting pairing.

In this paper, we construct the phase diagrams of the TI films with different magnetized and interacted TSSs by using a tight-binding (TB) model, within the same theoretical framework of the previous two-dimensional (2D) effective Hamiltonian [19,20]. In addition to the superconducting QAH, HPSQAH, and ZPQAH states with chiral MESs, we demonstrate the AI state, realized by the two TSSs without interaction but with antiferromagnetic exchange fields, can also host TSC phases characterized with a Chern number $N = 0$ and ± 1, where the $N = 0$ TSC phase hosts the helical MES without needing the π-phase difference in the superconducting gaps [17,19]. An intuitive understanding of TSC phase formation is given from the perspective of particle-hole symmetry that induces a sign change of Chern number, which enables one to find novel experimental platforms for realizing TSC with 1D MESs by directly analyzing band structures. The TSC phase diagrams in the parameter space of chemical potential (μ) and interacting strength (I) between two TSSs indicate that the $N = \pm 1$ TSC phase is robust against inter-TSS interaction when $(\Delta_b + \Delta_t)^2 \leqslant (Z_b + Z_t)^2$. Furthermore, we predict the $MnBi_2Te_4/Bi_2Te_3$ heterostructures coupled with conventional superconductivity to be an ideal experimental platform for realizing the $N = \pm 1$ TSC phase within a wide energy range (~80 meV) but without needing external magnetic field, using first-principles calculations. The chiral MESs are found to persist even in the cases with just one quintuple layer (QL) of Bi_2Te_3, consistent with the TB model analyses.

II. METHODS AND COMPUTATIONAL DETAILS

A. 2D TB model

It is well known that TSC phases can be induced in the TSSs [17–20] or the RSOCSs [21–23] coupled with s-wave superconductivity. The topological nontriviality stems from the spin-orbit coupling (SOC) term in the form of $\lambda(k_x\sigma_y - k_y\sigma_x)$ when $k_{x/y} \to 0$ for both cases. In addition to inducing the well-known Dirac cone with helical spin polarization that enables the formation of intraband spin-singlet superconducting pairing, SOC can be mapped onto the superconductivity part of Bogoliubov–de Gennes (BdG) Hamiltonian via a unitary transformation. The resulting effective superconducting gap $\Delta(k_x\sigma_y - k_y\sigma_x)$ possesses the form of a p-wave superconductivity, which is topological nontrivial when there are an odd number of time-reversal-invariant (TRI) momenta enclosed by an odd number of Fermi surface contours in the Brillouin zone (BZ) [46–48].

Consequently, we employ a two-orbital spin-full TB model with Rashba SOC in two triangle lattices locating,

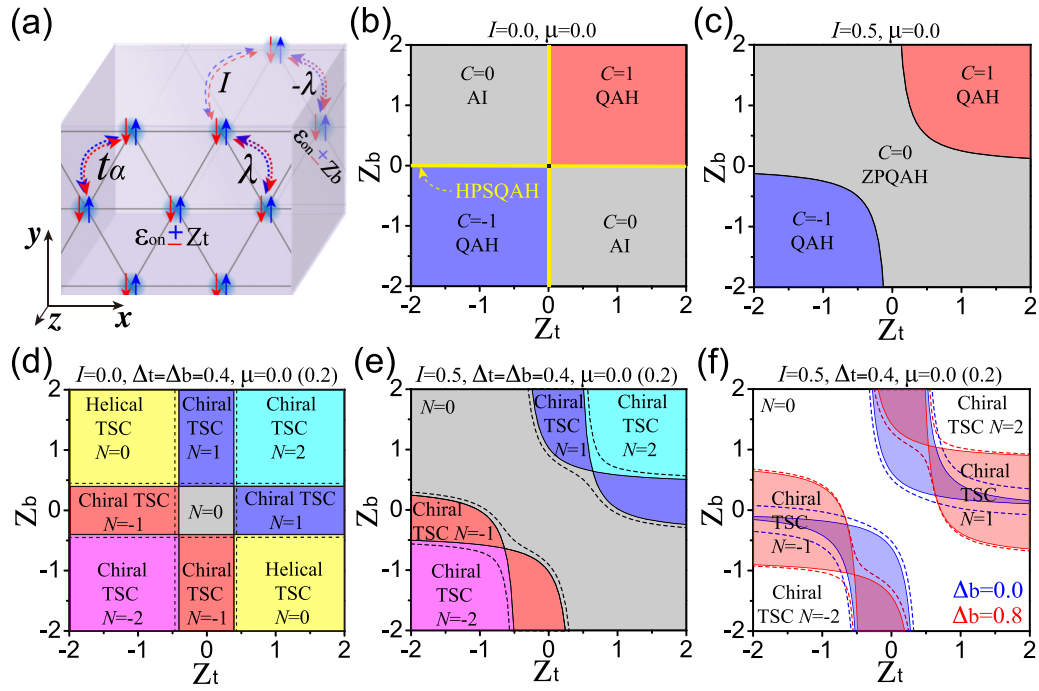

FIG. 2. (a) The schematic diagram of two-orbital TB model in a triangle lattice of orbitals locating, respectively, at top (front) and bottom (behind) surface of TI film. The phase diagrams of (b), (c) electronic states and (d)–(f) superconducting quasiparticles in the parameter space of Z_t and Z_b. The values of parameters used in the TB model are given in the corresponding figures. The dashed lines are plotted by using the values in the brackets to substitute the original ones.

respectively, at the top and bottom surface of a TI film [Fig. 2(a)], to construct the phase diagrams of the two TSSs with different exchange fields. The electronic Hamiltonian is written as

$$H = H_0 + H_R + H_Z + H_I, \tag{1}$$

$$H_0 = -t_\alpha \sum_{\langle m,n\rangle,\alpha} c^\dagger_{m\alpha} c_{n\alpha} + \text{H.c.} - \varepsilon_{on} \sum_{m,\alpha} c^\dagger_{m\alpha} c_{m\alpha}, \tag{2}$$

$$H_R = i\lambda \sum_{\langle m,n\rangle \in top,\alpha\neq\beta} \mathbf{e}_z(\boldsymbol{\sigma}^{\alpha\beta} \times \mathbf{d}_{mn}) c^\dagger_{m\alpha} c_{n\beta} - i\lambda \times \sum_{\langle m,n\rangle \in bottom,\alpha\neq\beta} \mathbf{e}_z(\boldsymbol{\sigma}^{\alpha\beta} \times \mathbf{d}_{mn}) c^\dagger_{m\alpha} c_{n\beta}, \tag{3}$$

$$H_Z = Z_t \sum_{m\in top,\alpha} c^\dagger_{m\alpha} \sigma_z^{\alpha\alpha} c_{m\alpha} + Z_b \sum_{m\in bottom,\alpha} c^\dagger_{m\alpha} \sigma_z^{\alpha\alpha} c_{m\alpha}, \tag{4}$$

$$H_I = I \sum_{\langle m,n\rangle_{inter},\alpha} c^\dagger_{m\alpha} c_{n\alpha} + \text{H.c.} \tag{5}$$

Here $c^\dagger_{m\alpha}$ and $c_{n\alpha}$ are creation and annihilation operators, respectively, for an electron with spin α on site m. t_α is the intrasurface nearest-neighbor hopping term. ε_{on} represents the onsite energy that moves the Dirac point to zero energy. H_R denotes the intrasurface nearest-neighbor Rashba SOC with the same strength λ for both surfaces, which can be deduced to the form of $\lambda(k_x\sigma_y - k_y\sigma_x)$ close to the Γ point. The $\mathbf{e}_z$ and $\mathbf{d}_{mn}$ are, respectively, the unit vector along the z direction and pointing from site n to m. $\boldsymbol{\sigma}$, σ_x, σ_y, and σ_z are the Pauli matrices for spin. H_Z corresponds to the exchange fields with Zeeman energy $Z_t(Z_b)$ being applied on top (bottom) surface by intrinsic magnetism [27,49–51] or magnetic proximity effect of FMIs [34–36]. H_I represents inter-TSS interaction with intersurface nearest-neighbor intraspin hopping magnitude I. The above parameters are labeled in Fig. 2(a) for clarity. The t_α is set to 1 and we assume λ equaling to 1 in both top and bottom surfaces for simplicity, because the magnitude of λ or different λ in top and bottom surfaces does not affect the Γ-point eigenvalues that determine the phase boundaries.

Rewriting the Hamiltonian of Eq. (1) in the momentum space as $H = \sum_{\mathbf{k}} \varphi^\dagger_{\mathbf{k}} h(\mathbf{k}) \varphi_{\mathbf{k}}$ with $\varphi_{\mathbf{k}} = (c^t_{\mathbf{k}\uparrow}, c^t_{\mathbf{k}\downarrow}, c^b_{\mathbf{k}\uparrow}, c^b_{\mathbf{k}\downarrow})^T$, the BdG Hamiltonian with the intraorbital spin-singlet pairing Δ condensing at μ was constructed under the basis of $\psi_{\mathbf{k}} = (c^t_{\mathbf{k}\uparrow}, c^t_{\mathbf{k}\downarrow}, c^b_{\mathbf{k}\uparrow}, c^b_{\mathbf{k}\downarrow}, c^{t\dagger}_{-\mathbf{k}\uparrow}, c^{t\dagger}_{-\mathbf{k}\downarrow}, c^{b\dagger}_{-\mathbf{k}\uparrow}, c^{b\dagger}_{-\mathbf{k}\downarrow})^T$:

$$H_{\text{BdG}} = \sum_{\mathbf{k}} \psi^\dagger_{\mathbf{k}} h_{\text{BdG}}(\mathbf{k}) \psi_{\mathbf{k}}, \tag{6}$$

$$h_{\text{BdG}}(\mathbf{k}) = \begin{pmatrix} h(\mathbf{k}) - \mu & \Delta \\ \Delta^\dagger & -h^*(-\mathbf{k}) + \mu \end{pmatrix}, \tag{7}$$

$$\Delta = \begin{pmatrix} i\Delta_t\sigma_y & 0 \\ 0 & i\Delta_b\sigma_y \end{pmatrix}. \tag{8}$$

Here the pairing gap opened on top/bottom TSS $\Delta_{t/b}$ can be induced by bulk superconductivity [9,10] or proximity/interface effect [6,7,52,53]. Here we focus on tuning the exchange fields (both direction and magnitude) while assume $\Delta_{t/b}$ to be both positive, since the dependence of phase diagram on phase difference of superconducting gaps were already discussed [19].

B. First-principles calculations

The Vienna *Ab initio* Simulation Package [54,55] was utilized to calculate the electronic property of the TSC candidate

materials, 1-septuple-layer (SL) $MnBi_2Te_4/n$QL-Bi_2Te_3 film, based on density-functional theory (DFT). The exchange-correlation functional was treated within the generalized gradient approximation in the form of Perdew-Burke-Ernzerhof [56]. The energy cutoff was set to 500 eV for plane-wave basis. A vacuum region of more than 15 Å was introduced to avoid the interactions between neighboring films subject to period boundary condition. Structural relaxation without SOC and self-consistent calculation with SOC were performed on a uniform $6 \times 6 \times 1$ **k**-point sampling of the first BZ, while a denser **k**-point sampling around Γ was employed to calculate the Zeeman gaps and spin expectation values. The van der Waals interaction, described by DFT-D3 functional with Becke-Jonson damping, was included, and the strong correlation effect of Mn 3 d electrons was taken into account by using the local spin-density approximations plus U method with $U = 6.0$ and $J = 1.0$ eV. The direction of magnetic moments (5 μB) of Mn^{2+} was set to be perpendicular to the 1SL-$MnBi_2Te_4/n$QL-Bi_2Te_3 film, since the out-of-plane ferromagnetism of the $MnBi_2Te_4$ SL was characterized experimentally in the $MnBi_2Te_4/Bi_2Te_3$ superlattice at low temperature [25,34].

To study the topological superconductivity of 1SL-$MnBi_2Te_4/n$QL-Bi_2Te_3-film, we employ the WANNIER90 package [57] to construct an electronic Hamiltonian $H_{\mathrm{MLWFs}}(\mathbf{k})$ using the basis of maximally localized Wannier functions (MLWFs) $\varphi_{\mathrm{MLWFs}} = (\varphi_{i\uparrow}, \varphi_{(i+\frac{\aleph}{2})\downarrow})^T$ by fitting the first-principles electronic states. Here $\aleph$ is the total number of MLWFs with the orbital index of $i = 1 \ldots \frac{\aleph}{2}$ and $i + \frac{\aleph}{2} = \frac{\aleph}{2} + 1 \ldots \aleph$ for up and down spin orbitals, respectively. The p orbitals of Bi and Te as well as d orbitals of Mn are used as the initial guess for the unitary transformations performed on a $12 \times 12 \times 1$ **k**-point mesh in the first BZ. The resulting first-principles BdG Hamiltonian $H^{\mathrm{BdG}}_{\mathrm{MLWFs}}(\mathbf{k})$ is expressed as

$$H^{\mathrm{BdG}}_{\mathrm{MLWFs}}(\mathbf{k}) = \begin{pmatrix} H_{\mathrm{MLWFs}}(\mathbf{k}) - (E_F + \mu) & \\ & -H^*_{\mathrm{MLWFs}}(-\mathbf{k}) + (E_F + \mu) \end{pmatrix} + H_\Delta, \tag{9}$$

$$H_\Delta = \Delta\left(\varphi^\dagger_{i\uparrow}\varphi^\dagger_{(i+\frac{\aleph}{2})\downarrow} - \varphi^\dagger_{(i+\frac{\aleph}{2})\downarrow}\varphi^\dagger_{i\uparrow}\right) + \Delta\left(\varphi_{(i+\frac{\aleph}{2})\downarrow}\varphi_{i\uparrow} - \varphi_{i\uparrow}\varphi_{(i+\frac{\aleph}{2})\downarrow}\right). \tag{10}$$

Details of this newly developed first-principles approach have been given previously [58]. The Chern number and 1D MESs are thus calculated from the solutions of Eqs. (9) and (10) to characterize the TSC phase. We also employ the WANNIER90 package to calculate the density of states (DOS) using an extremely dense **k**-point sampling ($500 \times 500 \times 1$) in the first BZ to ensure good convergence.

III. RESULTS AND DISCUSSION

A. Phase diagrams without and with superconductivity

We first construct the phase diagram without superconductivity in the parameter space of Z_t and Z_b by solving Eq. (1). The four eigenvalues at the Γ point are

$$E_1 = -\frac{1}{2}\left[(Z_t + Z_b) + \sqrt{4I^2 + (Z_t - Z_b)^2}\right],$$

$$E_2 = -\frac{1}{2}\left[(Z_t + Z_b) - \sqrt{4I^2 + (Z_t - Z_b)^2}\right],$$

$$E_3 = \frac{1}{2}\left[(Z_t + Z_b) - \sqrt{4I^2 + (Z_t - Z_b)^2}\right],$$

and

$$E_4 = \frac{1}{2}\left[(Z_t + Z_b) + \sqrt{4I^2 + (Z_t - Z_b)^2}\right]$$

[Figs. 1(b) and 1(c)]. Given the phase transition occurring at the gap closing point, the phase boundary is determined by setting $E_2 = E_3$, leading to $Z_tZ_b = I^2$. We calculated the Chern number at zero energy to be $C = 1/2 + 1/2 = 1$ for $Z_tZ_b > I^2$ and $C = 1/2 - 1/2 = 0$ for $Z_tZ_b < I^2$ under the basis of electronic wave functions, corresponding to the QAH state [Fig. 1(b)] and ZPQAH state [Fig. 1(c)] [27–29], respectively. If the TI film is thick enough to eliminate the inter-TSS interaction ($I = 0$), the AI state with $C = 0$ will emerge for $Z_tZ_b < 0$ [30–32], which is the special phase of ZPQAH state [Fig. 1(c)] that exhibits quantized topological magnetoelectric effect.

Moreover, when only one surface is under the exchange field, e.g., $Z_t \neq 0$ and $Z_b = 0$, the system is still gapped for $I \neq 0$, which fulfills the condition for the ZPQAH state, i.e., $I^2 > Z_tZ_b = 0$. For $I = 0$, one surface state possesses an exchange gap of $2Z_t$, while the other is gapless [Fig. 1(d)]. The gapped surface state has $C = 1/2$ within the exchange gap, corresponding to the HPSQAH state [19,20,26]. The phase diagrams without superconductivity are shown in Figs. 2(b) and 2(c) for $I = 0$ and $I \neq 0$, respectively, which clearly indicate the inter-TSSs interaction narrows the range of QAH state and converts the AI and HPSQAH states into ZPQAH state. Different phases may be induced by manipulating the thickness of TI film and the type of FMIs-TIs interfaces as well as the external magnetic field.

Next, the TSC phase diagrams of different magnetized and interacted TSSs with superconductivity were constructed by solving the TB BdG Hamiltonian H_{BdG} of Eq. (6). The phase boundaries of SC are determined by the closing points of bulk superconducting gap. We first consider the ideal case with perfect surface Dirac cones ($I = 0$) for thick TI films. The phase boundaries are given by $\sqrt{\Delta^2_{t/b} + \mu^2} = |Z_{t/b}|$. Our calculations show that the TSC phases with Chern number $N = \pm 1$ under the basis $\psi_{\mathbf{k}}$ emerge at

$$\begin{cases} \sqrt{\Delta_b^2 + \mu^2} < |Z_b| \\ \sqrt{\Delta_t^2 + \mu^2} > |Z_t| \end{cases} \quad \text{or} \quad \begin{cases} \sqrt{\Delta_b^2 + \mu^2} > |Z_b| \\ \sqrt{\Delta_t^2 + \mu^2} < |Z_t| \end{cases}.$$

For

$$\begin{cases} \sqrt{\Delta_b^2+\mu^2} < |Z_b| \\ \sqrt{\Delta_t^2+\mu^2} < |Z_t| \end{cases},$$

the Chern number is calculated as

$$N = \pm\frac{Z_tZ_b + |Z_tZ_b|}{Z_tZ_b}.$$

Bulk-boundary correspondence renders the chiral TSC phase with $N = \pm 1$ ($N = \pm 2$) to hold one (two) chiral MESs localizing at one edge, while $N = 0$ represents the TRI TSC phase featured with the helical MESs. There is also a trivial $N = 0$ superconductor phase when

$$\begin{cases} \sqrt{\Delta_b^2+\mu^2} > |Z_b| \\ \sqrt{\Delta_t^2+\mu^2} > |Z_t| \end{cases}.$$

We plot one example of the phase diagram in Fig. 2(d), which shows four critical points signifying the boundary of four phases. The nonzero chemical potential μ will not destroy these critical points but broaden the range of the $N = \pm 1$ TSC phases.

When TI films are not thick enough to eliminate the inter-TSS interaction, nonzero I and μ will remove the critical points, leading to a condition for phase boundaries as $I^2 + \Delta_0^2 + \mu^2 = Z_tZ_b \pm \sqrt{4I^2\mu^2 + (\Delta_0^2+\mu^2)(Z_t - Z_b)^2}$ when $\Delta_t = \Delta_b \equiv \Delta_0$. The phase diagram [Fig. 2(e)] clearly shows that the TSC phase can be induced even if $Z_t = Z_b$ and $\Delta_t = \Delta_b$. The formula can be deduced to $I^2 + \Delta_0^2 = Z_tZ_b \pm (Z_t - Z_b)\Delta_0$ for $\mu = 0$, similar to the previous report of assuming $\Delta_t \neq \Delta_b$ but $Z_t = Z_b$ [19]. This indicates that the superconducting and Zeeman gap play a similar role in forming the TSC phases. From Fig. 2(e), one can see that the inter-TSS interactions narrow the range of chiral TSC phases by converting the TRI TSC phase into a trivial phase. For $\Delta_t \neq \Delta_b$, the phase boundaries become complicated [Fig. 2(f)]. A general rule for $N = \pm 1$ TSC phase is that the range of $Z_{t/b}$ increases with the increase (decrease) of $\Delta_{t/b}(\Delta_{b/t})$, and can be further increased by nonzero μ.

Comparing the phase diagrams without [Figs. 2(b) and 2(c)] and with [Figs. 2(d)–2(f)] superconductivity, one can conclude that all the electronic phases formed by magnetizing the TSSs, i.e., QAH, HPSQAH, ZPQAH, are able to host the TSC phase with chiral MESs, consistent with previous reports [19,20]. Notably, the phase diagrams also reveal the existence of TRI TSC phase with helical MESs hosted by the AI state. The helical TSC phase stems from the opposite directions of exchange fields applied on two TSSs, similar to that realized in the two nanowires with opposite Zeeman splitting [59] and in the antiferromagnetic quantum spin Hall insulator [60]. Practically, this makes it possible to create TRI TSC phase without the need of unconventional superconductivity or two conventional superconductivity states with π-phase difference [17,19,61].

Next, we offer an intuitive explanation for the formation of TSC phase. It is known that Zeeman gap opening will induce opposite spin expectation values around the gap edges [Figs. 1(a)–1(d)], leading to nonzero Berry curvature. Integrating the Berry curvature of the gap-edge states will result in the Chern number of $C = \pm 1/2$. With μ being set at the energy marked in Figs. 1(a)–1(d), the dispersions of superconducting quasiparticles are plotted in Figs. 1(e)–1(h). The particle-hole symmetry of SCs ensures the opposite sign of Chern number for the eigenvalues distributed symmetrically with respect to the superconducting gap, as marked by the red ($C = 1/2$) and blue ($C = -1/2$) stars in Figs. 1(e)–1(h), respectively. Consequently, one can easily see that the superconducting gaps are all topological nontrivial with Chern number $N = 1$. The topological nontriviality is further confirmed by the existence of chiral MESs [Figs. 3(a) and 3(b)]. Similarly, if μ is set at the Zeeman gap around the Fermi level of the QAH [Fig. 1(b)] and AI [Fig. 1(c)] state, $N = \pm 2$ chiral and $N = 0$ helical TSC phases will emerge, which are demonstrated by the presence of two chiral MESs [Fig. 3(c)] and helical MESs [Fig. 3(d)], respectively.

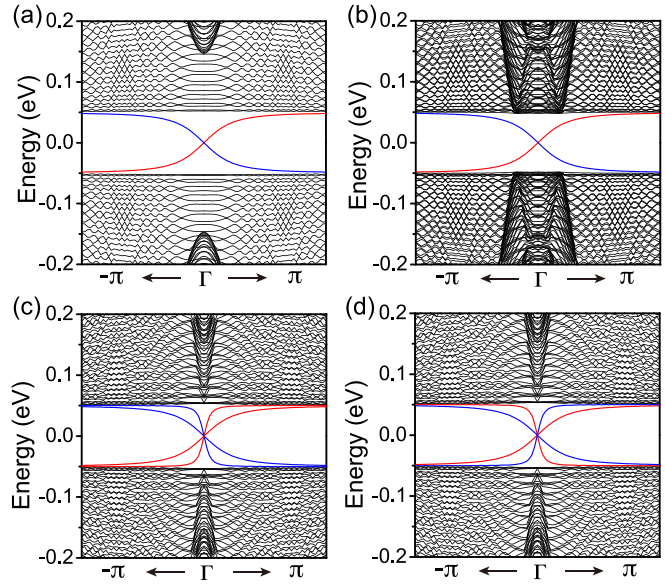

FIG. 3. The chiral MESs of the Chern number $N = 1$ TSC phase formed by the (a) RSOCSs and (b) the magnetized TSSs. (c) The double-chiral MESs of Chern number $N = 2$ TSC phase and (d) the helical MESs of Chern number $N = 0$ TRI TSC phase. The red (blue) color represents the MESs locating at the right (left) edge.

For specific TSC candidate experimental platforms, the exchange fields and superconducting gaps are usually fixed. A useful guidance for experiments would be to determine where the Fermi level should be so that the desired TSC phase can be induced, which also depends on the film thickness due to different strength (I) of inter-TSS interactions. We thus further construct the phase diagrams in the parameter space of μ and I, as shown in Fig. 4. Since the TSC phase boundary is set at $\mu^2 = Z_{t/b}^2 - \Delta_{t/b}^2$ when $I = 0$ [Fig. 2(d)], the condition for a solvable real μ is $Z_{t/b}^2 > \Delta_{t/b}^2$. We consider two scenarios with either both TSSs or only one TSS fulfilling this condition, respectively.

For the case of $\{\substack{Z_b^2 > \Delta_b^2 \\ Z_t^2 > \Delta_t^2}$ [Figs. 4(a) and 4(b)], the $N = \pm 2$ (or 0, TRI TSC), ± 1, and 0 phases emerge, respectively, at $-\sqrt{Z_{b/t}^2 - \Delta_{b/t}^2} < \mu < \sqrt{Z_{b/t}^2 - \Delta_{b/t}^2}$, $\sqrt{Z_{b/t}^2 - \Delta_{b/t}^2} < |\mu| < \sqrt{Z_{t/b}^2 - \Delta_{t/b}^2}$, and $|\mu| > \sqrt{Z_{t/b}^2 - \Delta_{t/b}^2}$ for $I = 0$ (here as-

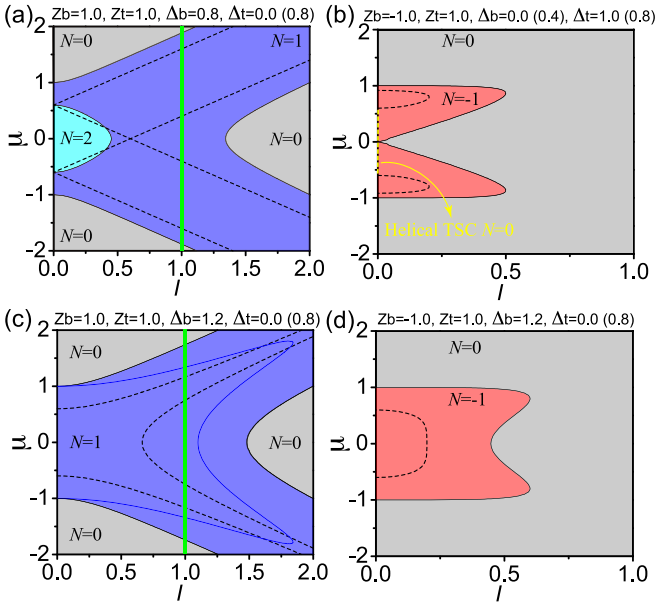

FIG. 4. The TSC phase diagram of superconducting quasiparticles with (a), (b) four or (c), (d) two solvable μ values when the two TSSs experiencing (a), (c) ferromagnetic or (b), (d) antiferromagnetic exchange fields. Detailed parameters are labeled in corresponding figures. The dashed lines are plotted by using the values in brackets to substitute the original values. The blue line in (c) is the TSC phase boundary of HPSQAH state with $Z_t = 1.0$, $Z_b = 0.0$, $\Delta_t = 0.0$, and $\Delta_b = 1.2$. Noting that the TSSs interaction will transfer the QAH state to ZPQAH state at $I^2 = Z_t Z_b$, as indicated by the green line in (a) and (c). The AI state exists in (b) and (d) when $I = 0$, and the rest of the parameter space corresponds to the ZPQAH state.

suming $Z_{t/b}^2 - \Delta_{t/b}^2 \geqslant Z_{b/t}^2 - \Delta_{b/t}^2$). When the two TSSs experience either the same or different ferromagnetic exchange fields [Fig. 4(a)], the $N = \pm 2$ TSC phase will transform into $N = \pm 1$ TSC and then to $N = 0$ trivial phases with the increasing I. The transition points with $\mu = 0$ are $I_1 = \sqrt{(Z_t + \Delta_t)(Z_b - \Delta_b)}$ and $I_2 = \sqrt{(Z_t - \Delta_t)(Z_b + \Delta_b)}$, respectively. The $N = \pm 2$ TSC phase only emerges from the QAH state, and the $N = \pm 1$ phase can be hosted by both the QAH and ZPQAH state, consistent with the phase diagrams in Fig. 2. The $N = 0$ trivial and $N = \pm 2$ TSC phases may transform into each other by changing μ when $Z_{t/b}^2 - \Delta_{t/b}^2 = Z_{b/t}^2 - \Delta_{b/t}^2$ or changing I when $\{^{\Delta_b = \Delta_t}_{Z_b = Z_t}$ [see dashed lines in Fig. 4(a)]. For the ZPQAH and AI states formed by the two TSSs with antiferromagnetic exchange fields [Fig. 4(b)], the $N = 0$ helical TSC phase is destroyed together with the disappearance of AI when $I \neq 0$, and the largest I for the $N = \pm 1$ TSC phase is

$$I_3 = \frac{1}{2}\sqrt{\frac{\left(\Delta_b^2 - \Delta_t^2 - Z_b^2 + Z_t^2\right)^2}{(\Delta_b + \Delta_t)^2 - (Z_b + Z_t)^2}}$$

with

$$\mu_3^{\pm} = \pm\frac{\sqrt{4(\Delta_t Z_b - \Delta_b Z_t)^2 - [(\Delta_b + \Delta_t)^2 - (Z_b + Z_t)^2]^2}}{2\sqrt{(\Delta_b + \Delta_t)^2 - (Z_b + Z_t)^2}}.$$

For the case of $\{^{Z_b^2 < \Delta_b^2}_{Z_t^2 > \Delta_t^2}$ [Figs. 4(c) and 4(d)], there are only two real solutions for μ. The $N = \pm 1$ phase exists at $-\sqrt{Z_t^2 - \Delta_t^2} < \mu < \sqrt{Z_t^2 - \Delta_t^2}$ for $I = 0$, while the $N = \pm 2$ chiral and $N = 0$ helical TSC phases are absent for the ferromagnetic [Fig. 4(c)] and antiferromagnetic [Fig. 4(d)] exchange fields being applied on the TSSs, respectively. The phase translation point in Fig. 4(c) between the $N = \pm 1$ TSC and $N = 0$ trivial phases is I_1 or I_2 when $\mu = 0$, and the largest I for the $N = \pm 1$ TSC phase in Fig. 4(d) is I_3 with $\mu_3^{\pm}$, same as the cases with four solvable μ.

Notably, the phase diagrams indicate that the $N = \pm 1$ TSC phase is robust against the increasing I when the two TSSs are under ferromagnetic exchange fields [Figs. 4(a) and 4(c)]. The robustness is manifested in two aspects. One is that the range of μ will be enlarged by a larger I due to the enhanced spin splitting of $E_{4/2} - E_{3/1} = \sqrt{4I^2 + (Z_b - Z_t)^2}$ for QAH state [Fig. 1(b)]. The other is that the range of μ remains nearly constant when further increasing the I. This is because the spin splitting of $E_{3/1} - E_{4/2} = Z_b + Z_t$ does not depend on the I for ZPQAH state [Fig. 1(c)]. Actually, the condition of realizing such robust $N = \pm 1$ TSC is the absence of solvable real I_3, which can be deduced to be $(\Delta_b + \Delta_t)^2 \leqslant (Z_b + Z_t)^2$.

B. TSC candidate materials

From the experimental perspective, a large range of μ will ease the detection of the TSC phase. One can clearly see from Fig. 4 that the valid range of μ for the $N = \pm 1$ phase can be extended to the Zeeman gap edge of the TSS with zero superconducting gap, and reaches the upper limit when the Zeeman gap in the other TSS is smaller than the superconducting gap. We suggest the optimal choice for realizing $N = \pm 1$ phase is $Z_{t/b} \neq 0$, $\Delta_{t/b} = 0$, $Z_{b/t} \leqslant \Delta_{b/t}$, and $\Delta_{b/t} \neq 0$ (assuming $Z_{t/b} \geqslant Z_{b/t} \geqslant 0$). Previous theoretical work proposed a special case of this criterion using the parameter of $Z_{t/b} \neq 0$, $\Delta_{t/b} = 0$, $Z_{b/t} = 0$, and $\Delta_{b/t} \neq 0$ [20], which, however, is limited by the precondition that the decay length of the exchange field is smaller than the film thickness to ensure $Z_{b/t} = 0$. Our calculations indicate that this precondition is not necessary because the condition of $Z_{b/t} \neq 0$ can be beneficial for further enlarging the range of μ [see the blue line in Fig. 4(c)], within which the TSC phase resides. Thus, our work opens up opportunity to realize $N = \pm 1$ TSC phase in ultrathin TI films.

In addition to a larger range of μ for detecting the TSC phase, a simpler material platform would benefit experiments. We suggest a better choice for realizing the $N = \pm 1$ phases by constructing an FMI/TI-film/SC heterostructure. The thickness-dependent decay length of exchange field and coherence length of superconductivity may lead to different superconducting and Zeeman gaps that open in the two TSSs of TI film. Specifically, we propose a heterostructure composed of Bi_2Te_3 film and FMI $MnBi_2Te_4$ SL as a candidate platform for observing the chiral MESs, which have already been fabricated and show large magnetic gap at the Dirac point of TSSs [25,34]. The ingredient of superconductivity can be provided by interfacing $MnBi_2Te_4/Bi_2Te_3$ with SC $NbSe_2$ [6,7] and FeTe [52,53], or possibly even by applying external pressure using diamond-anvil cell technique [62].

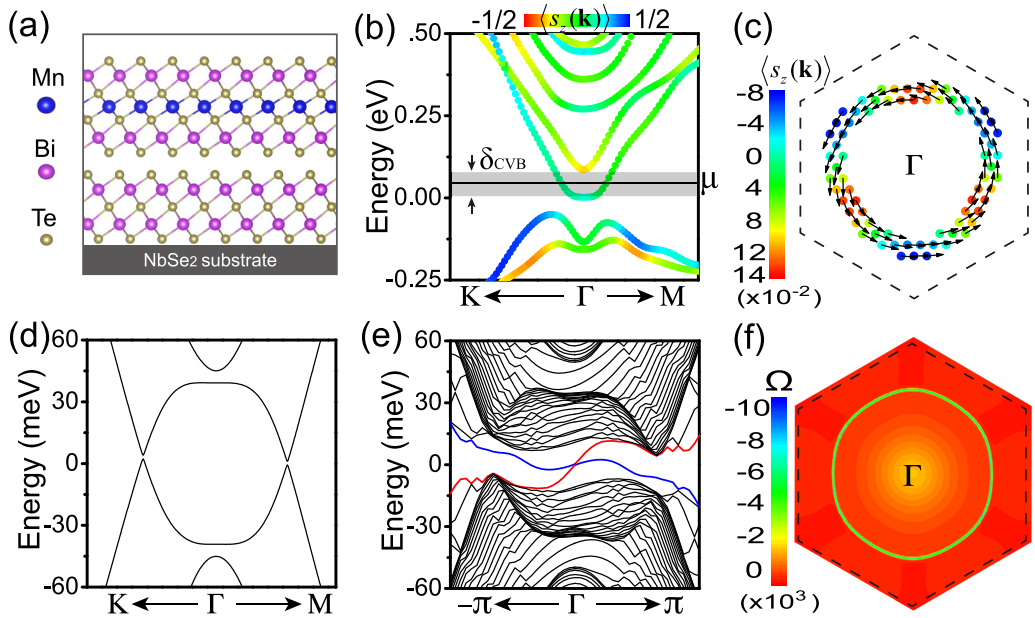

FIG. 5. (a) The side view and (b) the electronic band structure of 1SL-$MnBi_2Te_4$/1QL-Bi_2Te_3 grown on SC $NbSe_2$. The black shadow in (b) represents the δ_{CVB} that can realize the $N = \pm 1$ TSC phase. (c) The constant energy contours at the energy μ labeled by solid black line in (b); the black arrows and colored dots represent the in-plane and out-of-plane components of electron spin expectation values, respectively. (d) The dispersion of superconducting quasiparticles in 1SL-$MnBi_2Te_4$/1QL-Bi_2Te_3 calculated by using the first-principles BdG Hamiltonian with the superconducting gap of 1.0 meV condensing at the μ. (e) The dispersion of quasiparticles in the 1SL-$MnBi_2Te_4$/1QL-Bi_2Te_3 nanoribbon with the width of 250 primitive cells. Here the superconducting gap was magnified by 10× to show the chiral MESs (red and blue lines) more clearly. (f) The total Berry curvature distribution near the Γ point for the states below the superconducting gap.

Below, we elaborate further on the case of the proximity effect with $NbSe_2$.

We first consider the heterostructure of 1SL-$MnBi_2Te_4$/1QL-Bi_2Te_3-film [Fig. 5(a)]. The magnetic proximity effect of FMI $MnBi_2Se_4$ SL breaks the time-reversal symmetry, leading to a band structure with spin degeneracy lifted [Fig. 5(b)]. We focus on the potential TSC phase formed by the conduction valley bands (CVB), since the experimentally fabricated Bi_2Te_3 film tends to be n doped and the CVB will finally transfer to TSSs when the Bi_2Te_3 film is thick enough [63]. For convenience, we define the exchange gap of the interested band as the energy difference between the two spin-polarized states at the Γ point, e.g., the exchange gap δ_{CVB} (δ_{TSS}) of CVB (TSS) labeled in Fig. 5(b) [Fig. 6(a)]. For the electronic states within the δ_{CBV} of 1SL-$MnBi_2Te_4$/1QL-Bi_2Te_3 film [Fig. 5(b)], the out-of-plane components of spin expectation values are negligible because of a strong SOC strength. The dominant in-plane components have the so-called helical spin texture with opposite spin expectation values at **k** and **–k** point [Fig. 5(c)], respectively, which ensures the precondition for a spin-singlet superconductivity pairing. Here we should emphasize that the magnetic proximity effect of FMIs does not hinder the superconducting proximity effect since the induced out-of-plane components have also opposite directions at **k** and **–k** point [Fig. 5(c)].

To characterize the topological nontriviality of superconductivity, we employ the electronic Hamiltonian $H_{\mathrm{MLWFs}}(\mathbf{k})$ of 1SL-$MnBi_2Te_4$/1QL-Bi_2Te_3 film to construct a first-principles BdG Hamiltonian $H^{\mathrm{BdG}}_{\mathrm{MLWFs}}(\mathbf{k})$ through Eqs. (9) and (10), where the superconducting gap of Δ∼1.0 meV [6] is assumed to open at the μ labeled in Fig. 5(b). The dispersion of superconducting quasiparticles [Fig. 5(d)] calculated by diagonalizing the $H^{\mathrm{BdG}}_{\mathrm{MLWFs}}(\mathbf{k})$ clearly shows that a superconducting gap is opened, whose topological nontriviality is demonstrated by the existence of chiral MESs [Fig. 5(e)]. To better understand the origin of TSC phase, we calculated the Berry curvature of all the quasiparticle states below the superconducting gap using $H^{\mathrm{BdG}}_{\mathrm{MLWFs}}(\mathbf{k})$. The result shows that the Berry curvature is mainly located at those **k** points where the superconducting gap opens [Fig. 5(f)], which is different from the case of ideal TSSs and RSOCS when Berry curvature is mainly located at those points where the Zeeman gap opens [58]. This again demonstrates that the superconducting and Zeeman gap can act similarly to form the TSC phase. Integrating the Berry curvature over the first BZ leads to a Chern number of $N = -1$, indicating the 1SL-$MnBi_2Te_4$/1QL-Bi_2Te_3 film indeed hosts robust chiral MESs upon becoming superconducting, in the absence of external magnetic field and with nonideal (gapped) TSSs. The topological nontriviality remains robust as long as μ is located inside the exchange gap δ_{CVB} [Fig. 5(b)], providing a wide energy range (∼80 meV) for realizing TSC.

With the increase of Bi_2Te_3-film thickness, the CVB gradually transforms into a Dirac-cone-like dispersion starting from 4QL-Bi_2Te_3 film [Fig. 6(a)], indicating the formation of TSSs, which is consistent with the previous experimental reports [64,65]. The Chern numbers N of 1SL-$MnBi_2Te_4$/4QL-Bi_2Te_3 film with conventional superconductivity are then calculated by constructing the first-principles $H^{\mathrm{BdG}}_{\mathrm{MLWFs}}(\mathbf{k})$, which demonstrate that the $N = \pm 1$

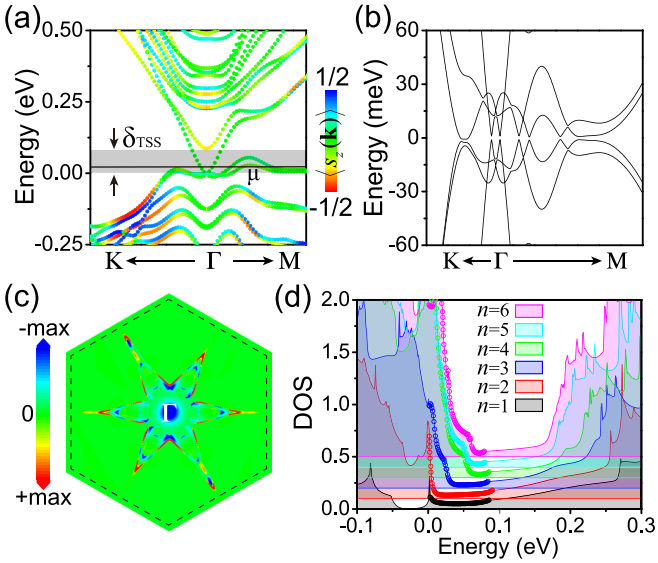

FIG. 6. (a) The electronic band structure of 1SL-$MnBi_2Te_4$/4QL-Bi_2Te_3. The colors represent the z component of spin expectation values. The black shadow represents the range of δ_{TSS} within which the $N = \pm 1$ TSC phase can be realized. (b) The dispersion of superconducting quasiparticles with the superconducting gap of 1.0 meV opening at the μ labeled in (a). (c) The total Berry curvature distribution near the Γ point for the states below the superconducting gap. (d) The DOS curve of 1SL-$MnBi_2Te_4$/nQL-Bi_2Te_3 film with $n = 1$, 2, 3, 4, 5, and 6. The circles represent the electronic states that can realize the $N = \pm 1$ TSC phase.

TSC phase can be induced when the superconducting gap opens inside the exchange gap δ_{TSS}. One representative result is shown in Fig. 6(b), where one can clearly see that a superconducting gap is fully opened, with the Chern number N being well defined and calculated to be -1 by integrating the Berry curvature [Fig. 6(c)]. The result also indicates that the bulk states, despite overlapping with the TSSs, do not affect the topological nontriviality of superconducting quasiparticles.

To better guide the experimental detection of the predicted TSC phases, we further suggest a way to benchmark whether the Fermi level lies within the range of TSC phase, by inspecting the shape of the DOS curve, instead of carrier concentration, as done for Bi_2Te_3/$NbSe_2$ heterostructure [7]. The DOS for 1SL- $MnBi_2Te_4$/nQL-Bi_2Te_3 film is plotted in Fig. 6(d), with the electronic states that form the $N = \pm 1$ TSC phase being marked by the circles. One sees clearly that all the cases considered possess a wide energy range (∼80 meV) of realizing the TSC phase. The upper bound of the energy range is determined by the inflection point in the DOS curve occurring at the edge of the exchange gap in TSS. On the other hand, close to the lower bound, the DOS increases gradually due to the overlap between TSSs and bulk states in thick Bi_2Te_3 films. Therefore, by comparing the shape of the calculated and experimentally measured DOS curves, such as by scanning tunneling spectroscopy, one will be able to judge if the Fermi level is located inside the energy window of the TSC phase or estimate how much carrier doping is needed to move it into the window. Then the TSC phase could be confirmed by performing electronic transport measurement, and the smoking-gun evidence of chiral MESs, e.g., half-integer conductance plateau ($e^2/2h$) [11,19] and the oscillation of critical Josephson current [66], are expected to be detected in the 1SL-$MnBi_2Te_4$/nQL-Bi_2Te_3 film.

Finally, since fabrication of TI/FMI heterostructures is well developed [25,33–45], magnetizing both TSSs simultaneously in a sandwich FMI/TI/FMI heterostructure provides a promising way to realize all the predicted TSC phases with different Chern numbers (Fig. 2). The electronic and magnetic properties of some candidate systems, including CrI_3/Bi_2Se_3/CrI_3 [24], $MnBi_2Se_4$/Bi_2Se_3/$Mn_2Bi_2Se_5$ [31], and CrI_3/Bi_2Se_3/$MnBi_2Se_4$ [32], have been studied already. Based on the intuitive understanding of the TSC phase mentioned above, we propose that all these three heterostructures interfaced with a conventional superconductor can realize the $N = 0$ helical, $N = \pm 1$, and $N = \pm 2$ chiral TSC phase by properly adjusting the Fermi levels. To detect the desired TSC phases, experiments should synthesize high-quality material platforms and ensure an out-of-plane ferromagnetism in the FMIs, as done for $MnBi_2Te_4$/Bi_2Te_3 superlattice at low temperature [25,34]. Otherwise, e.g., the substitutional Mn resultant in-plane magnetization in Mn-doped Bi_2Se_3 [34] may make the TSC phases difficult to be induced. Meanwhile, in addition to the 1SL-$MnBi_2Te_4$/Bi_2Te_3 − film/1SL-$Mn_2Bi_2Te_5$ heterostructure, we suggest growth of thick $MnBi_2Te_4$ film (not calculated) on $NbSe_2$ substrate as a candidate material to realize the $N = 0$ helical and $N = \pm 2$ chiral TSC phases. The thick $MnBi_2Te_4$ film is an antiferromagnetic TI that exhibits the AI (QAH) state with even (odd) number SLs [27,49–51]. The combination of a large exchange gap (60 ∼ 100 meV) of $MnBi_2Te_4$ [27] and a small superconducting gap (∼1.0 meV) of $NbSe_2$ [6] should make the $MnBi_2Te_4$-film/$NbSe_2$ suitable for observing the helical or the double-chiral MESs, over a wide range of μ (the range of exchange gap), by changing the thickness of $MnBi_2Te_4$ film. Electronic transport measurement performed on this material platform should present an integer conductance plateau of e^2/h when double-chiral MESs are present, while the existence of helical MESs may be confirmed if the conductance gradually increases from e^2/h to $2e^2/h$ when the lead moves toward the superconductor [60].

IV. CONCLUSION

Motivated by the recently fabricated various heterostructures consisting of TIs and FMIs, we developed extended phase diagrams of magnetized TSSs together with conventional superconductivity, based on TB model analyses. In addition to reproducing previous reports, our calculations indicate that the helical MES can be realized by the AI state by exploiting different Zeeman gaps, instead of the previously proposed π-phase difference of the superconducting gaps in the TSSs. An intuitive understanding for the formation of TSC phases is given from the perspective of particle-hole symmetry that induces a sign change of Chern number, which enables one to design experimental platforms for realizing TSC by directly analyzing band structures. We also

demonstrate that the TSC phase is robust against the increase of interaction between two TSSs when the thickness of TI film is reduced. Using first-principles approach, we predict 1SL-$MnBi_2Te_4$/nQL-Bi_2Te_3 film with superconducting proximity effect to be an ideal candidate TSC material platform with Chern number $N = -1$, where the chiral MESs persist even down to one QL Bi_2Te_3.

ACKNOWLEDGMENTS

X.Z. acknowledges financial support by the National Natural Science Foundation of China (Grant No. 12004357) and the Young Talents Project at Ocean University of China (Grant No. 862001013185). F.L. acknowledges financial support from National Science Foundation Quantum Leap Big Idea under Grant No. 1936383.

[1] C. Nayak, S. H. Simon, A. Stern, M. Freedman, and S. D. Sarma, Rev. Mod. Phys. **80**, 1083 (2008).
[2] A. Y. Kitaev, Ann. Phys. **303**, 2 (2003).
[3] B. Lian, X.-Q. Sun, A. Vaezi, X.-L. Qi, and S.-C. Zhang, Proc. Natl. Acad. Sci. USA **115**, 10938 (2018).
[4] R. M. Lutchyn, E. P. A. M. Bakkers, L. P. Kouwenhoven, P. Krogstrup, C. M. Marcus, and Y. Oreg, Nat. Rev. Mater. **3**, 52 (2018).
[5] S. Nadj-Perge, I. K. Drozdov, J. Li, H. Chen, S. Jeon, J. Seo, A. H. MacDonald, B. A. Bernevig, and A. Yazdani, Science **346**, 602 (2014).
[6] J.-P. Xu, C. Liu, M.-X. Wang, J. Ge, Z.-L. Liu, X. Yang, Y. Chen, Y. Liu, Z.-A. Xu, C.-L. Gao, D. Qian, F.-C. Zhang, and J.-F. Jia, Phys. Rev. Lett. **112**, 217001 (2014).
[7] J.-P. Xu, M.-X. Wang, Z.-L. Liu, J.-F. Ge, X. Yang, C. Liu, Z.-A. Xu, D. Guan, C.-L. Gao, D. Qian, Y. Liu, Q.-H. Wang, F.-C. Zhang, Q.-K. Xue, and J.-F. Jia, Phys. Rev. Lett. **114**, 017001 (2015).
[8] B. Jäck, Y. Xie, J. Li, S. Jeon, B. A. Bernevig, and A. Yazdani, Science **364**, 1255 (2019).
[9] S. Zhu, L. Kong, L. Cao, H. Chen, M. Papaj, S. Du, Y. Xing, W. Liu, D. Wang, C. Shen, F. Yang, J. Schneeloch, R. Zhong, G. Gu, L. Fu, Y.-Y. Zhang, H. Ding, and H.-J. Gao, Science **367**, 189 (2020).
[10] Y.-F. Lv, W.-L. Wang, Y.-M. Zhang, H. Ding, W. Li, L. Wang, K. He, C.-L. Song, X.-C. Ma, and Q.-K. Xue, Sci. Bull. **62**, 852 (2017).
[11] Q. L. He, L. Pan, A. L. Stern, E. C. Burks, X. Che, G. Yin, J. Wang, B. Lian, Q. Zhou, E. S. Choi, K. Murata, X. Kou, Z. Chen, T. Nie, Q. Shao, Y. Fan, S.-C. Zhang, K. Liu, J. Xia, and K. L. Wang, Science **357**, 294 (2017).
[12] G. C. Ménard, S. Guissart, C. Brun, R. T. Leriche, M. Trif, F. Debontridder, D. Demaille, D. Roditchev, P. Simon, and T. Cren, Nat. Commun. **8**, 2040 (2017).
[13] A. Palacio-Morales, E. Mascot, S. Cocklin, H. Kim, S. Rachel, D. K. Morr, and R. Wiesendanger, Sci. Adv. **5**, eaav6600 (2019).
[14] S. Kezilebieke, Md N. Huda, V. Vaňo, M. Aapro, S. C. Ganguli, O. J. Silveira, S. Głodzik, A. S. Foster, T. Ojanen, and P. Liljeroth, Nature (London) **588**, 424 (2020).
[15] Z. Wang, J. O. Rodriguez, L. Jiao, S. Howard, M. Graham, G. D. Gu, T. L. Hughes, D. K. Morr, and V. Madhavan, Science **367**, 104 (2020).
[16] W. Wang, S. Kim, M. Liu, F. A. Cevallos, R. J. Cava, and N. P. Ong, Science **368**, 534 (2020).
[17] L. Fu and C. L. Kane, Phys. Rev. Lett. **100**, 096407 (2008).
[18] X.-L. Qi, T. L. Hughes, and S.-C. Zhang, Phys. Rev. B **82**, 184516 (2010).
[19] J. Wang, Q. Zhou, B. Lian, and S.-C. Zhang, Phys. Rev. B **92**, 064520 (2015).
[20] J. J. He, T. Liang, Y. Tanaka, and N. Nagaosa, Commun. Phys. **2**, 149 (2019).
[21] M. Sato, Y. Takahashi, and S. Fujimoto, Phys. Rev. Lett. **103**, 020401 (2009).
[22] J. D. Sau, S. Tewari, R. M. Lutchyn, T. D. Stanescu, and S. D. Sarma, Phys. Rev. B **82**, 214509 (2010).
[23] J. D. Sau, R. M. Lutchyn, S. Tewari, and S. Das Sarma, Phys. Rev. Lett. **104**, 040502 (2010).
[24] Y. Hou, J. Kim, and R. Wu, Sci. Adv. **5**, eaaw1874 (2019).
[25] H. Deng, Z. Chen, A. Wołoś, M. Konczykowski, K. Sobczak, J. Sitnicka, I. V. Fedorchenko, J. Borysiuk, T. Heider, Ł. Pluciński, K. Park, A. B. Georgescu, J. Cano, and L. Krusin-Elbaum, Nature Physics, doi:10.1038/s41567-020-0998-2 (2020).
[26] J. Maciejko, X.-L. Qi, H. D. Drew, and S.-C. Zhang, Phys. Rev. Lett. **105**, 166803 (2010).
[27] M. M. Otrokov, I. P. Rusinov, M. Blanco-Rey, M. Hoffmann, A. Y. Vyazovskaya, S. V. Eremeev, A. Ernst, P. M. Echenique, A. Arnau, and E. V. Chulkov, Phys. Rev. Lett. **122**, 107202 (2019).
[28] J. Wang, B. Lian, and S.-C. Zhang, Phys. Rev. B **89**, 085106 (2014).
[29] J. Wang, B. Lian, X.-L. Qi, and S.-C. Zhang, Phys. Rev. B **92**, 081107(R) (2015).
[30] D. Xiao, J. Jiang, J.-H. Shin, W. Wang, F. Wang, Y.-F. Zhao, C. Liu, W. Wu, M. H. W. Chan, N. Samarth, and C.-Z. Chang, Phys. Rev. Lett. **120**, 056801 (2018).
[31] Y. Hou and R. Wu, Nano Lett. **19**, 2472 (2019).
[32] Y. S. Hou, J. W. Kim, and R. Q. Wu, Phys. Rev. B **101**, 121401(R) (2020).
[33] C. Gong and X. Zhang, Science **363**, eaav4450 (2019).
[34] E. D. L. Rienks, S. Wimmer, J. Sánchez-Barriga, O. Caha, P. S. Mandal, J. Růžička, A. Ney, H. Steiner, V. V. Volobuev, H. Groiss, M. Albu, G. Kothleitner, J. Michalička, S. A. Khan, J. Minár, H. Ebert, G. Bauer, F. Freyse, A. Varykhalov, O. Rader, and G. Springholz, Nature (London) **576**, 423 (2019).
[35] T. Hirahara, S. V. Eremeev, T. Shirasawa, Y. Okuyama, T. Kubo, R. Nakanishi, R. Akiyama, A. Takayama, T. Hajiri, S.-i. Ideta, M. Matsunami, K. Sumida, K. Miyamoto, Y. Takagi, K. Tanaka, T. Okuda, T. Yokoyama, S.-i. Kimura, S. Hasegawa, and E. V. Chulkov, Nano Lett. **17**, 3493 (2017).
[36] A. V. Matetskiy, I. A. Kibirev, T. Hirahara, S. Hasegawa, A. V. Zotov, and A. A. Saranin, Appl. Phys. Lett. **107**, 091604 (2015).
[37] A. Kandala, A. Richardella, D. W. Rench, D. M. Zhang, T. C. Flanagan, and N. Samarth, Appl. Phys. Lett. **103**, 202409 (2013).
[38] W. Yang, S. Yang, Q. Zhang, Y. Xu, S. Shen, J. Liao, J. Teng, C. Nan, L. Gu, Y. Sun, K. Wu, and Y. Li, Appl. Phys. Lett. **105**, 092411 (2014).

[39] Y. Wang, D. Zhu, Y. Wu, Y. Yang, J. Yu, R. Ramaswamy, R. Mishra, S. Shi, M. Elyasi, K.-L. Teo, Y. Wu, and H. Yang, Nat. Commun. **8**, 1364 (2017).
[40] P. Wei, F. Katmis, B. A. Assaf, H. Steinberg, P. Jarillo-Herrero, D. Heiman, and J. S. Moodera, Phys. Rev. Lett. **110**, 186807 (2013).
[41] S. Zhu, D. Meng, G. Liang, G. Shi, P. Zhao, P. Cheng, Y. Li, X. Zhai, Y. Lu, L. Chen, and K. Wu, Nanoscale **10**, 10041 (2018).
[42] L. D. Alegria, H. Ji, N. Yao, J. J. Clarke, R. J. Cava, and J. R. Petta, Appl. Phys. Lett. **105**, 053512 (2014).
[43] Z. Jiang, C.-Z. Chang, C. Tang, P. Wei, J. S. Moodera, and J. Shi, Nano Lett. **15**, 5835 (2015).
[44] C. Tang, C.-Z. Chang, G. Zhao, Y. Liu, Z. Jiang, C.-X. Liu, M. R. McCartney, D. J. Smith, T. Chen, J. S. Moodera, and J. Shi, Sci. Adv. **3**, e1700307 (2017).
[45] M. Mogi, T. Nakajima, V. Ukleev, A. Tsukazaki, R. Yoshimi, M. Kawamura, K. S. Takahashi, T. Hanashima, K. Kakurai, T.-h. Arima, M. Kawasaki, and Y. Tokura, Phys. Rev. Lett. **123**, 016804 (2019).
[46] M. Sato, Phys. Rev. B **79**, 214526 (2009).
[47] M. Sato, Phys. Rev. B **81**, 220504(R) (2010).
[48] L. Fu and E. Berg, Phys. Rev. Lett. **105**, 097001 (2010).
[49] M. M. Otrokov, I. I. Klimovskikh, H. Bentmann, D. Estyunin, A. Zeugner, Z. S. Aliev, S. Gaß, A. U. B. Wolter, A. V. Koroleva, A. M. Shikin, M. Blanco-Rey, M. Hoffmann, I. P. Rusinov, A. Y. Vyazovskaya, S. V. Eremeev, Y. M. Koroteev, V. M. Kuznetsov, F. Freyse, J. Sánchez-Barriga, I. R. Amiraslanov, M. B. Babanly, N. T. Mamedov, N. A. Abdullayev, V. N. Zverev, A. Alfonsov, V. Kataev, B. Büchner, E. F. Schwier, S. Kumar, A. Kimura, L. Petaccia, G. Di Santo, R. C. Vidal, S. Schatz, K. Kißner, M. Ünzelmann, C. H. Min, S. Moser, T. R. F. Peixoto, F. Reinert, A. Ernst, P. M. Echenique, A. Isaeva, and E. V. Chulkov, Nature (London) **576**, 416 (2019).
[50] C. Liu, Y. Wang, H. Li, Y. Wu, Y. Li, J. Li, K. He, Y. Xu, J. Zhang, and Y. Wang, Nat. Mater. **19**, 522 (2020).
[51] Y. Deng, Y. Yu, M. Z. Shi, Z. Guo, Z. Xu, J. Wang, X. H. Chen, and Y. Zhang, Science **367**, 895 (2020).
[52] Q. L. He, H. Liu, M. He, Y. H. Lai, H. He, G. Wang, K. T. Law, R. Lortz, J. Wang, and I. K. Sou, Nat. Commun. **5**, 4247 (2014).
[53] H. Qin, B. Guo, L. Wang, M. Zhang, B. Xu, K. Shi, T. Pan, L. Zhou, J. Chen, Y. Qiu, B. Xi, I. K. Sou, D. Yu, W.-Q. Chen, H. He, F. Ye, J.-W. Mei, and G. Wang, Nano Lett. **20**, 3160 (2020).
[54] G. Kresse and J. Furthmüller, Phys. Rev. B **54**, 11169 (1996).
[55] G. Kresse and J. Hafner, Phys. Rev. B **48**, 13115 (1993).
[56] J. P. Perdew, K. Burke, and M. Ernzerhof, Phys. Rev. Lett. **77**, 3865 (1996).
[57] A. A. Mostofi, J. R. Yates, Y.-S. Lee, I. Souza, D. Vanderbilt, and N. Marzari, Comput. Phys. Commun. **178**, 685 (2008).
[58] X. Zhang, K.-H. Jin, J. Mao, M. Zhao, Z. Liu, and F. Liu, arXiv:2004.04890v2.
[59] C. Reeg, C. Schrade, J. Klinovaja, and D. Loss, Phys. Rev. B **96**, 161407(R) (2017).
[60] Y. Huang and C.-K. Chiu, Phys. Rev. B **98**, 081412(R) (2018).
[61] A. Haim and Y. Oreg, Phys. Rep. **825**, 1 (2019).
[62] J. L. Zhang, S. J. Zhang, H. M. Weng, W. Zhang, L. X. Yang, Q. Q. Liu, S. M. Feng, X. C. Wang, R. C. Yu, L. Z. Cao, L. Wang, W. G. Yang, H. Z. Liu, W. Y. Zhao, S. C. Zhang, X. Dai, Z. Fang, and C. Q. Jin, Proc. Natl. Acad. Sci. USA **108**, 24 (2011).
[63] H. Zheng and J.-F. Jia, Chin. Phys. B **28**, 67403 (2019).
[64] Y. Liu, G. Bian, T. Miller, M. Bissen, and T. C. Chiang, Phys. Rev. B **85**, 195442 (2012).
[65] Y.-Y. Li, G. Wang, X.-G. Zhu, M.-H. Liu, C. Ye, X. Chen, Y.-Y. Wang, K. He, L.-L. Wang, X.-C. Ma, H.-J. Zhang, X. Dai, Z. Fang, X.-C. Xie, Y. Liu, X.-L. Qi, J.-F. Jia, S.-C. Zhang, and Q.-K. Xue, Adv. Mater. **22**, 4002 (2010).
[66] C.-Z. Chen, J. J. He, D.-H. Xu, and K. T. Law, Phys. Rev. B **98**, 165439 (2018).